Detailed analytical approach to the Gaussian surface bidirectional reflectance distribution function specular component applied to the sea surface

3 authors, including:

Denis Dion
Defence Research and Development Canada
51 PUBLICATIONS   318 CITATIONS

SEE PROFILE

Guy Potvin
Defence Research and Development Canada
31 PUBLICATIONS   180 CITATIONS

SEE PROFILE

OSA STATEMENT

Detailed analytical approach to the Gaussian surface bidirectional reflectance distribution function specular component applied to the sea surface

Vincent Ross

AEREX Avionique Inc., 36 du Ruisseau, Suite 102, Breakeyville, Quebec, Canada, G0S 1E2

Denis Dion and Guy Potvin

Defense Research and Development of Canada, Valcartier, 2459 Pie-XI Boulevard, Val-Bélair, Quebec, Canada, G3J 1X5

A statistical sea surface specular BRDF (bidirectional reflectance distribution function) model is developed that includes mutual shadowing by waves, wave facet hiding, and projection weighting. The integral form of the model is reduced to an analytical form by making minor and justifiable approximations. The new form of the BRDF thus allows one to compute sea reflected radiance more than 100 times faster than the traditional numerical solutions. The repercussions of the approximations used in the model are discussed. Using the analytical form of the BRDF, an analytical approximation is also obtained for the reflected sun radiance that is always good to within 1% of the numerical solution for sun elevations of more than 10° above the horizon. The model is validated against measured sea radiances found in the literature and is shown to be in very good agreement. © 2005 Optical Society of America

OCIS codes: 010.4450, 030.6600, 080.2720, 000.5490.

1. INTRODUCTION

In the context of remote sensing applications or detection studies in marine environments, a precise theoretical model to determine the sea surface bidirectional reflectance distribution function (BRDF) is often crucial. Such a model is required to determine effectively the radiance reflected or emitted from the sea surface. Sea reflectance is usually described as the sum of a specular component generated at the air–water interface, a whitecap contribution, and the underlight emitted or scattered from under the surface. The specular component of the reflectance has been the subject of much controversy because of the difficulties in describing the rough surface and the strong directional nature of its interaction with impinging radiation.

The specular component of the BRDF can be modeled in many ways, each having advantages and drawbacks. The method that is usually considered to be the most accurate uses a Monte Carlo approach to create many random three-dimensional (3D) instances of the sea surface.[1–4] Hundreds, or even thousands of rays are then traced from a source to a detector for each instance of the surface. The results obtained are then averaged into an overall reflectance, and ultimately into radiance. High accuracy can be obtained as shadows, hiding of waves by other waves, and multiple scattering are all naturally taken into account, making a limited amount of simplifications and assumptions. The drawback of this detailed calculation is long computational time, undesirable for most applications other than academic research.

A much faster and popular method of calculating the BRDF basically involves the convolution of Fresnel reflectances with the probabilities of a source actually being reflected toward the receiver. Although quicker, this basic approach has many physical limitations since the effects manifested by a true 3D surface are overlooked. These shortcomings become clear when trying to reproduce actual observations. For example Su *et al.*[5] highlighted features in their measurements that cannot be reproduced using this simple model alone. Nevertheless, it is possible to account for some of these effects by altering the slope probability-density functions (PDF) using shadowing and hiding functions. However, adding these corrections slows down computation significantly since it often involves solving a number of embedded numerical integrals.

In order to maintain the desired level of physical correctness while obtaining reasonable computation times, many different approximations can be used. Zeisse[6,7] managed to find an analytical expression for calculating sea reflectance including some amount of hiding and weighting, but the nature of his approximations limits the use of the expression to grazing angles only. In another example, Mermelstein *et al.*[8] developed a method using a number of small angle and small slope approximations along with parametric fits to many of the physical quantities to calculate radiances quickly. Again, some of the

approximations yield inaccurate results in some reflection geometries.[9]

The need for rapid computation of accurate sea radiance demands a better solution. In this paper, we propose a solution to the BRDF equations that eliminates the need for any numerical integration while including as much physical correctness as practical. The result is a significant reduction in sea radiance computation time, with no intrinsic limitations on reflection geometries. The model is then applied to reproduce cases presented by Su *et al.*,[5] and simulations are shown to be in very good agreement with measurements. Other implications of having an analytic solution are also discussed.

2. GEOMETRICAL CONSIDERATIONS

The spherical coordinate system is the most natural in order to localize the source to be reflected and the receiver with reference to a surface element, or facet (see Fig. 1). The elevation angle origin is chosen to be at the zenith, since the horizon may vary because of refraction. Because of the symmetry of the slope PDF with the wind direction (see Section 3), the upwind direction is chosen as the azimuth origin. In some calculations, it is also convenient to define a Cartesian coordinate system in order to represent some important quantities as vectors to which linear algebra can be applied. This latter system is aligned with the polar system with the z axis pointing toward the zenith and the x axis in the upwind direction. It is therefore useful for expressing relevant quantities using both these coordinate systems, and to define transformation relationships that will permit us to move easily from one coordinate system to the other. Definitions of geometrical quantities used in this paper are given in Fig. 1.

The unit vectors $\mathbf{U}_i = (x_i, y_i, z_i)(i = n, r, s)$ are defined in the Cartesian coordinate system according to their polar coordinates (θ, ϕ_i) so that
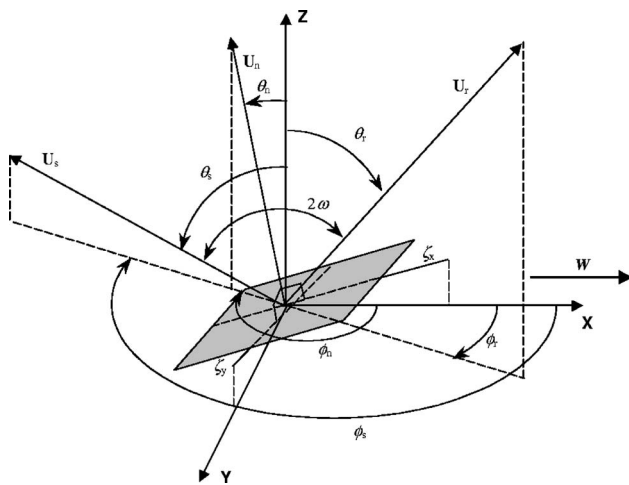

Fig. 1. Coordinate system and representations of relevant quantities: $\mathbf{U}_n$, facet Cartesian normal unit vector; $\mathbf{U}_r$, receiver Cartesian unit vector; etc. $\mathbf{U}_s$, source Cartesian unit vector; ω, reflection angle; θ_i, zenith angle of $\mathbf{U}_i$ vector $(i = n, r, s)$; ϕ_i, azimuth angle of $\mathbf{U}_i$ vector $(i = n, r, s)$ counterclockwise from upwind direction $(\mathbf{W})$ ζ_x, facet slope in the upwind $(\mathbf{W})$ direction ζ_y, facet slope in the crosswind direction.

$$\begin{pmatrix} x_i \\ y_i \\ z_i \end{pmatrix} = \begin{pmatrix} \sin\theta_i \cos\phi_i \\ \sin\theta_i \sin\phi_i \\ \cos\theta_i \end{pmatrix}, \tag{1}$$

and the inverse transformation is done with

$$\theta_i = \cos^{-1}(z_i),$$

$$\phi_i = \tan^{-1}(y_i/x_i). \tag{2}$$

In Eqs. (1) and (2), the subscript n represents the facet normal while s and r are for the source and receiver quantities, respectively. It is also useful to link the facet normal unit vector to the upwind- and crosswind-projected slopes (ζ_x, ζ_y) of the facet. This is done with the relation

$$\begin{pmatrix} x_n \\ y_n \\ z_n \end{pmatrix} = \frac{1}{\sqrt{1 + \zeta_x^2 + \zeta_y^2}} \begin{pmatrix} -\zeta_x \\ -\zeta_y \\ 1 \end{pmatrix}, \tag{3}$$

with the inverse relation being

$$\zeta_x = -x_n/z_n,$$

$$\zeta_y = -y_n/z_n. \tag{4}$$

In this coordinate system, a specular reflection on a facet is defined by the law of reflection, which connects the facet normal to the source and receiver vectors such that

$$\mathbf{U}_s = 2\cos(\omega)\mathbf{U}_n - \mathbf{U}_r, \tag{5a}$$

$$\omega = \cos^{-1}(\mathbf{U}_r \cdot \mathbf{U}_n), \tag{5b}$$

$$\Rightarrow \mathbf{U}_s = 2(\mathbf{U}_r \cdot \mathbf{U}_n)\mathbf{U}_n - \mathbf{U}_r, \tag{5c}$$

where ω is the incidence angle (also equal to the reflection angle) defined as the angle between the receiver unit vector and the surface normal. By using Eq. (1) on $\mathbf{U}_s$ its spherical coordinates can then be found. Inversely, the sea slope geometry necessary to reflect a source with a known position can be determined with

$$\zeta_x = -\frac{(x_r + x_s)}{(z_r + z_s)}, \tag{6a}$$

$$\zeta_y = -\frac{(y_r + y_s)}{(z_r + z_s)}. \tag{6b}$$

Note that even in the presence of refraction and earth curvature, this geometry is still valid because it is all defined at the point of interaction on the facet surface. Whenever possible, slopes and angular quantities will be represented as vectors such that $\mathbf{\Psi}_i = (\theta_i, \phi_i)_{i=n,r,s}$ and $\boldsymbol{\zeta} = (\zeta_x, \zeta_y)$.

3. SEA SURFACE STATISTICS

The basis of a statistical description of sea surface reflectance is necessarily a statistical model of the surface itself. One of the first such models was pioneered by Cox and Munk[10,11] when they used a Gram–Charlier expansion whose first-order term is the Gaussian

$$p_0(\zeta|U) = \frac{1}{2\pi\sigma_x\sigma_y} \exp\left\{-\frac{1}{2}\left(\frac{\zeta_x^2}{\sigma_x^2} + \frac{\zeta_y^2}{\sigma_y^2}\right)\right\} \qquad (7)$$

to describe the sea slope PDF. Additional terms correct for kurtosis (peakedness) and skewness:

$$p \approx p_0\left\{1 - \frac{1}{2}c_{21}(Y^2-1)X - \frac{1}{6}c_{03}(X^3-3X) + \frac{1}{24}c_{40}(Y^4-6Y^2 \right.$$
$$\left. +3) + \frac{1}{4}c_{22}(Y^2-1)(X^2-1) + \frac{1}{24}c_{04}(X^4-6X^2+3)\right\}, \quad (8)$$

where

$$X = \zeta_x/\sigma_x, \quad Y = \zeta_y/\sigma_y.$$

In Eqs. (7) and (8), U is the wind speed at 12.5 m while σ_x^2 and σ_y^2 are the upwind and crosswind variances. The coefficients in relation (8) along with the variances depend on wind speed. Through observations of sun glint photographs, the variances were found by Cox and Munk to be given by

$$\sigma_x^2 = 0.003\,16U \quad \pm 0.004, \qquad (9a)$$

$$\sigma_y^2 = 0.003 + 0.001\,92U \quad \pm 0.004. \qquad (9b)$$

As noted by Cox and Munk, the alignment of the PDF major axes with the wind direction is a result of the capillary and small-scale, locally generated gravity waves' being the principal contributors to the slope statistics.

The Cox and Munk skewness expansion coefficients in relation (8) are given by

$$c_{21} = 0.01 - 0.0086U, \quad c_{03} = 0.04 - 0.033U, \qquad (10)$$

while the kurtosis coefficients are

$$c_{40} = 0.40, \quad c_{22} = 0.12, \quad c_{04} = 0.23. \qquad (11)$$

Other expressions linking the crosswind and upwind variances with wind speed have been published since the work of Cox and Munk. A reanalysis of the Cox and Munk data by Wu[12,13] showed that a two-branch logarithmic expression could represent a better fit to their measurements. Using a wave height spectral power density spectrum, other expressions can also be derived,[8,14,15] but wave slope variances obtained in this fashion proved consistently larger compared with direct measurements and are usually too large to produce accurate simulations using statistical models such as ours.[16,17] Some scientists have attempted to correlate the variances with other environmental parameters such as atmospheric stability or swell conditions. Hwang and Shemdin[18] found that although the state of swell development had some influence, it was small compared with the effect of atmospheric stability. This was confirmed by Shaw and Churnside[19] who added their data to that of Hwang and Shemdin and obtained an expression modifying Cox and Munk's variances according to stability:

$$\frac{\sigma_{sc}^2}{\sigma_{cm}^2} = \begin{cases} 1.42 - 2.80Ri, & -0.23 < Ri < 0.27 \\ 0.65, & Ri \geqslant 0.27 \end{cases} . \qquad (12)$$

In this equation, Ri is a reduced Richardson number, an index of air stability above the sea surface:

$$Ri = g\frac{\Delta T_{a-w}z}{T_w U_z^2}, \qquad (13)$$

where g is the gravitational constant (9.8 ms^{-2}), T_w is the sea surface temperature (°C), ΔT_{a-w} is the air–water temperature difference (°C), and U_z is the wind speed at the same measurement height z as the air temperature (10 m in the case of Shaw and Churnside).

We can now define the occurrence probability P that a wave facet will have horizontally projected slopes within $\pm d\zeta_x/2$ of ζ_x and $\pm d\zeta_y/2$ of ζ_y using the PDF so that

$$P \equiv p(\zeta|U)d^2\zeta. \qquad (14)$$

Also, since a PDF must always be normalized to unity,

$$\int_{-\infty}^{\infty}\int_{-\infty}^{\infty} p(\zeta|U)d^2\zeta = 1. \qquad (15)$$

In the simplest model, statistically averaged quantities over all possible wave slopes are then obtained by a convolution in slope space with Eq. (14) so that

$$\bar{F} = \int_{-\infty}^{\infty}\int_{-\infty}^{\infty} F(\zeta)p(\zeta|U)d^2\zeta, \qquad (16)$$

where $F(\zeta)$ is usually either the emissivity of the facet with slopes ζ_x and ζ_y multiplied by the blackbody function, or the reflectance of the facet multiplied by the incident radiance of the source being reflected.

For conciseness, hereafter all dependence on wind speed will be implicit for all quantities that have any dependence on the slope variances.

4. VISIBLE INTERACTION PROBABILITY

Although Eq. (16) can be used to obtain a sea surface BRDF, it lacks much in the way of physical correctness. Some of the facets in the integration are either hidden from the receiver or are in shadow with respect to a source, and thus cannot contribute to the overall radiance. Furthermore, the facets that the receiver does see are most likely tilted to some varying degree and do not all contribute equally.

In order to account for these effects, we must no longer simply consider the probability that a given facet orientation will occur; we must consider that there can actually be an interaction between the receiver, the radiance exiting a facet, if it is not an emission but a reflection, and in this case an incident ray. This idea was brought forth by Plass *et al.*,[20] who defined the interaction probability

$$Q \equiv q(\zeta|\Psi)d^2\zeta \qquad (17)$$

that a facet whose slope is within $\pm d\zeta_x/2$ of ζ_x and $\pm d\zeta_y/2$ of ζ_y will occur and have an interaction with a ray arriving from the arbitrary direction Ψ. In what follows, we

add a slight nuance to this concept by defining the visible interaction probability

$$Q_v \equiv q_v(\zeta|\boldsymbol{\Psi}_r, \boldsymbol{\Psi}_s)\mathrm{d}^2\zeta \qquad (18)$$

to clarify the fact that the interaction with an incident ray must also be visible from the receiver's standpoint.

We distinguish three types of functions that transform p into q_v. These are the weighting functions W that account for facet tilt, the hiding functions H that eliminate facets that the receiver cannot see, and the shadowing functions S that darken facets that a source cannot illuminate. The visible interaction probability q_v is then proportional to the product $p \cdot W \cdot H \cdot S$. Note that S is not involved in the calculation of emissivity since there is no dependence on an external source.

A. Facet Projection Weighting
Since facets that have their normals oriented exactly toward the receiver will have greater influence on radiance than those that are tilted away to some degree, a weighting function must be introduced. Zeisse[6,7] showed that this function is given by

$$W(\boldsymbol{\zeta}, \boldsymbol{\Psi}_r) = \frac{\cos \omega}{\cos \theta_n} = \frac{\mathbf{U}_n \cdot \mathbf{U}_r}{z_n}, \qquad (19)$$

where θ_n and ω are calculated from both receiver and facet geometry.

B. Slope Hiding and Shadowing
The hiding function that accounts for not seeing the backside of a wave is relatively straightforward since we either see it or we do not. It is simply given by

$$H_\zeta(\boldsymbol{\zeta}, \boldsymbol{\Psi}_r) = \Upsilon(\mathbf{U}_n \cdot \mathbf{U}_r), \qquad (20)$$

where Υ is the Heaviside function and is defined as

$$\Upsilon(x) = \begin{cases} 0, & x \leq 0 \\ 1, & x > 0 \end{cases}. \qquad (21)$$

Symmetrically, shadowing is defined in just the same way using the source geometry instead, with an additional term to account for the fact that all points below the horizon are shadowed by the horizon itself

$$S_\zeta(\boldsymbol{\zeta}, \boldsymbol{\Psi}_s) = \Upsilon(\mathbf{U}_n \cdot \mathbf{U}_s)\Upsilon(\pi/2 - \theta_s). \qquad (22)$$

Strictly speaking, $\Upsilon(\mathbf{U}_n \cdot \mathbf{U}_s)$ should be included in the BRDF when the source position is arbitrary. However, when used in the context of Eq. (16), it is always equal to 1 since the source position is calculated directly from the reflection geometry.

C. Wave Hiding and Shadowing
Just as the Heaviside function was chosen to hide the backside of waves, the Smith wave-height-hiding function[21,22] can be used to account for hiding by other waves. It is given by

$$H_w(h, \boldsymbol{\Psi}_r) = \left[1 - \frac{1}{2}\mathrm{erfc}(h) \right]^{\Lambda(v_r)}, \qquad (23a)$$

$$\Lambda(v_r) = \frac{\exp(-v_r^2) - v_r\sqrt{\pi}\,\mathrm{erfc}(v_r)}{2v_r\sqrt{\pi}}, \qquad (23b)$$

$$v_r = \frac{\cot(\theta_r)}{\sqrt{2}\sigma(\phi_r)}, \qquad (23c)$$

where h is the facet height, erfc is the complementary error function $(1 - \mathrm{erf})$ and $\sigma(\phi_r)$ is the slope variance in direction ϕ_r and is calculated from

$$\sigma^2(\phi_r) = \sigma_x^2 \cos^2 \phi_r + \sigma_y^2 \sin^2 \phi_r. \qquad (24)$$

The Smith shadowing function is chosen over the Wagner[23] shadowing function because it includes an additional normalization factor. The Smith function has also been shown to produce better results when compared with Monte Carlo simulations (Bourlier *et al.*[2]). The hiding of facets by other waves implies that we must have some statistical knowledge of the height of the facets and their correlation to slopes. However, in the case where height and slope distributions are uncorrelated, which is a reasonable approximation according to Bourlier *et al.*,[2] this is unnecessary. This is simply because no matter what part of the wave is hidden, the part that the receiver sees will have the exact same statistical description and will contribute in the same way to the radiance. Because of this, wave hiding on its own is meaningless for an uncorrelated surface.

By symmetry, the wave shadowing function will have the exact same form as Eq. (23), but with source geometry parameters instead:

$$S_w(h, \boldsymbol{\Psi}_s) = \left[1 - \frac{1}{2}\mathrm{erfc}(h) \right]^{\Lambda(v_s)}, \qquad (25a)$$

$$\Lambda(v_s) = \frac{\exp(-v_s^2) - v_s\sqrt{\pi}\,\mathrm{erfc}(v_s)}{2v_s\sqrt{\pi}}, \qquad (25b)$$

$$v_s = \frac{\cot(\theta_s)}{\sqrt{2}\sigma(\phi_s)}. \qquad (25c)$$

The shadowing function does not have a valid physical significance when used on its own because whether or not a facet is in shadow, the receiver must still see it in order for it to contribute to the radiance. Therefore, only the product $S_w(h, \boldsymbol{\Psi}_s)H_w(h, \boldsymbol{\Psi}_r)$ has actual physical implications.

Because of wave shadowing, a dependence on facet height has been added to the visible interaction probability. Assuming that slope and height are uncorrelated, one can show that[3]

$$q_v(\zeta, h|\boldsymbol{\Psi}_r, \boldsymbol{\Psi}_s) = q_v(\zeta|\boldsymbol{\Psi}_r)q_v(h|\boldsymbol{\Psi}_r, \boldsymbol{\Psi}_s), \qquad (26a)$$

$$q_v(\zeta|\boldsymbol{\Psi}_r) = [p(\zeta)W(\zeta, \boldsymbol{\Psi}_r)H_\zeta(\zeta, \boldsymbol{\Psi}_r)], \qquad (26b)$$

$$q_v(h|\boldsymbol{\Psi}_r, \boldsymbol{\Psi}_s) = [p(h)S_w(h, \boldsymbol{\Psi}_s)H_w(h, \boldsymbol{\Psi}_r)], \qquad (26c)$$

where the height distribution is modeled as an independent random variable with a Gaussian PDF of

$$p(h) = \frac{1}{\sigma_h \sqrt{2\pi}} \exp\left(\frac{h^2}{2\sigma_h^2}\right). \qquad (27)$$

The uncorrelated slope and height assumption also permits us to eliminate the dependence of h in q. Since the height of the facet does not by itself affect the actual capability of the facet to emit or reflect as long as the source can illuminate it, and because a facet in a receiver field of view can be of any height, we can use height integrated values so that Eq. (26) becomes

$$q_v(\zeta|\Psi_r, \Psi_s) = q_v(\zeta|\Psi_r) \int_{-\infty}^{\infty} q_v(h|\Psi_r, \Psi_s). \qquad (28)$$

D. Normalization

Because of weighting, shadowing, and hiding, many facets are rejected and the property imposed in Eq. (15) is violated. To correct this, normalization must be applied so that

$$q_{vn}(\zeta|\Psi_r, \Psi_s) = \frac{q_v(\zeta|\Psi_r)}{\displaystyle\int_{-\infty}^{\infty}\int_{-\infty}^{\infty} q_v(\zeta|\Psi_r)\mathrm{d}^2\zeta}$$
$$\times \frac{\displaystyle\int_{-\infty}^{\infty} q_v(h|\Psi_r, \Psi_s)\mathrm{d}h}{\displaystyle\int_{-\infty}^{\infty} p(h)H_w(h, \Psi_r)\mathrm{d}h}. \qquad (29)$$

Here, only the hiding and weighting functions are included in the normalization because the receiver can still see shadowed facets, even though they do not contribute positively to the radiance. This expression applies only to the calculation of the reflected energy. When there is no source dependence (thermal emission contribution), shadowing functions must be taken out of the expression. When this is done, one notes that the height integrals cancel each other out. This shows that wave-height hiding has no importance in emissivity calculations for a Gaussian surface with no correlation between slope and height.

5. ANALYTICAL RESULT

Calculating Eq. (29) numerically can be a lengthy process because of multiple integrations. This is even more apparent when used in the context of Eq. (16) to calculate radiance where five embedded integrations must be performed. Even if we neglect wave-height hiding, as is usually the case, calculating the normalizing factor is still time-consuming. According to Sancer,[24] the integration of the product of the Smith shadowing function and a Gaussian height distribution function can be done with the geometrical optics approximation and yields

$$\int_{-\infty}^{\infty} p(h)H_w(h, \Psi_r)\mathrm{d}h = \int_{-\infty}^{\infty} p(h)\left[1 - \frac{1}{2}\,\mathrm{erfc}(h)\right]^{\Lambda(v_r)} \mathrm{d}h$$
$$= \frac{1}{1 + \Lambda(v_r)}. \qquad (30)$$

The expression for $\Lambda(v_r)$ is given in Eq. (23). The analyti-

cal integration in the presence of both the wave hiding and shadowing functions is analogous:

$$\int_{-\infty}^{\infty} q_v(h|\Psi_r, \Psi_s)\mathrm{d}h = \int_{-\infty}^{\infty} p(h)S_w(h, \Psi_s)H_w(h, \Psi_r)\mathrm{d}h$$
$$= \int_{-\infty}^{\infty} p(h)\left[1 - \frac{1}{2}\,\mathrm{erfc}(h)\right]^{\Lambda(v_r)+\Lambda(v_s)} \mathrm{d}h$$
$$= \frac{1}{1 + \Lambda(v_r) + \Lambda(v_s)}. \qquad (31)$$

Only the slope integral of the denominator of the visible interaction probability density remains to be solved. We found that the normalization factor can be expressed using an analytic form as

$$\int_{-\infty}^{\infty}\int_{-\infty}^{\infty} q_v(\zeta|\Psi_r)\mathrm{d}^2\zeta \simeq \int_{-\infty}^{\infty}\int_{-\infty}^{\infty} p_0(\zeta)W(\zeta, \Psi_r)H_\zeta(\zeta, \Psi_r)\mathrm{d}^2\zeta$$
$$= [1 + \Lambda(v_r)]\cos(\theta_r), \qquad (32)$$

when the Gaussian approximation of Eq. (7) is used instead of the Gram–Charlier expansion. Since the demonstration of Eq. (32) is rather formal, it is relegated to Appendix A. Using this solution, along with Eqs. (30) and (31), the normalized visible interaction probability of Eq. (29) can be rewritten as

$$q_{vn}(\zeta|\Psi_r, \Psi_s) = \left[\frac{1 + \Lambda(v_r)}{1 + \Lambda(v_r) + \Lambda(v_s)}\right]\frac{p(\zeta)W(\zeta, \Psi_r)H_\zeta(\zeta, \Psi_r)}{[1 + \Lambda(v_r)]\cos\theta_r}, \qquad (33a)$$

$$= \frac{p(\zeta)W(\zeta, \Psi_r)H_\zeta(\zeta, \Psi_r)}{[1 + \Lambda(v_r) + \Lambda(v_s)]\cos\theta_r}, \qquad (33b)$$

$$= \frac{p(\zeta)W(\zeta, \Psi_r)H_\zeta(\zeta, \Psi_r)}{[1 + \Lambda(v_r)]\cos\theta_r}. \qquad (33c)$$

The fraction in square brackets in Eq. (33a) is the integrated combined wave shadowing and hiding function and is always equal to 1 in the calculation of the radiant thermal energy (see Subsection 4.D). Because of this, the form of Eq. (33b) is used when reflecting a source and Eq. (33c) is used in thermal emission calculations. Note that in Eqs. (33), the complete Gram–Charlier expansion for the occurrence probability of relation (8) is used in the numerator instead of the Gaussian approximation although the Gaussian approximation is made to simplify the denominator. This is justified because there are more differences in single values of the functions than in the integrated values. The impact of this approximation is discussed further in Section 6.

6. DISCUSSION

In our model, shadowed waves are considered to be completely dark if shadowed from a given point source. This is not quite true in reality because the facet may reflect another facet that can see the source. The result will be a systematic underestimation of the average reflectance.

Yet, including these multiple reflections would slow the algorithm exponentially with each additional reflection. We can attempt to estimate the impact of this approximation. It has been estimated by Preisendorfer *et al.*[1] and Henderson *et al.*[4] that 10 to 15% of the rays that arrive at a detector have been reflected more than once. Since the average reflectance (albedo) of water is never much greater than 20% (Jin *et al.*[25]), the error should not exceed 2 to 3% with the largest errors occurring at high wind speeds, low sun elevations, and near horizontal detector orientations.

In Fig. 2, we see that the extent of the error caused by using the Gaussian PDF approximation in the normalizing factor does not exceed 3%, even for relatively high wind speeds. The analytical expressions of Eqs. (33) slightly violate Eq. (15) but the computational speed advantage of having an analytical solution greatly outweighs the error. In studying Fig. 3, it becomes clear that the approximated analytical result in Eqs. (33) is much closer to the exact numerical solution computed with Gram–Charlier expansions than by using only Gaussians. The approximation violating Eq. (15) thus seems a better alternative than using Gaussian approximations to remain mathematically correct.

It is worth noting that the numerical results shown in Fig. 3 were obtained with very-high-resolution quadratures, which are thousands of times slower than the analytical computation. If the quadratures are brought to more reasonable speeds, the numerical errors become at least as large as for the analytical approximation, even if the full Gram–Charlier expansion is used. This is evident from Table 1 where the computational speeds are compared at equal precision (averaged down the center of the glint pattern from the horizon to the nadir). The speed difference is smaller for high wind speeds since the analytical model becomes less precise. Even so, for wind speeds most commonly found over the world's oceans, one can expect a computational speed gain factor ranging between 100 and 500 when using the analytical BRDF model. A simple bilinear quadrature (trapezoid rule) was considered adequate for this comparison, although it cannot be considered optimal. Note that the gains in Table 1 are not fully representative of the gain for the overall radiance computation, as more calculations than the BRDF come into play. Even when considering these factors, we expect the speed gain to remain substantial.

New developments in sea slope PDF characterization from Plant[26] may eventually lead to a fully consistent analytical form obeying Eq. (15). In his study, the Gram–Charlier representation in the upwind direction is shown to be closely matched by the sum of two Normal distributions that relate to the statistics of bound and free waves, respectively. Apart from having an interesting physical interpretation, this form for the PDF gives rise to an analytical solution of Eq. (32) and a mathematically exact analytical solution for Eqs. (33). Unfortunately, this approach remains impractical until a parametrization of the slope statistics with environmental conditions is available in the bound–free-wave representation that agrees well with observations.

Since Eqs. (30) and (31) are solved using the geometrical optics approximation, the solution given here is restricted to wavelengths smaller than the smallest wave structures. By balancing the rate of energy loss due to vis-
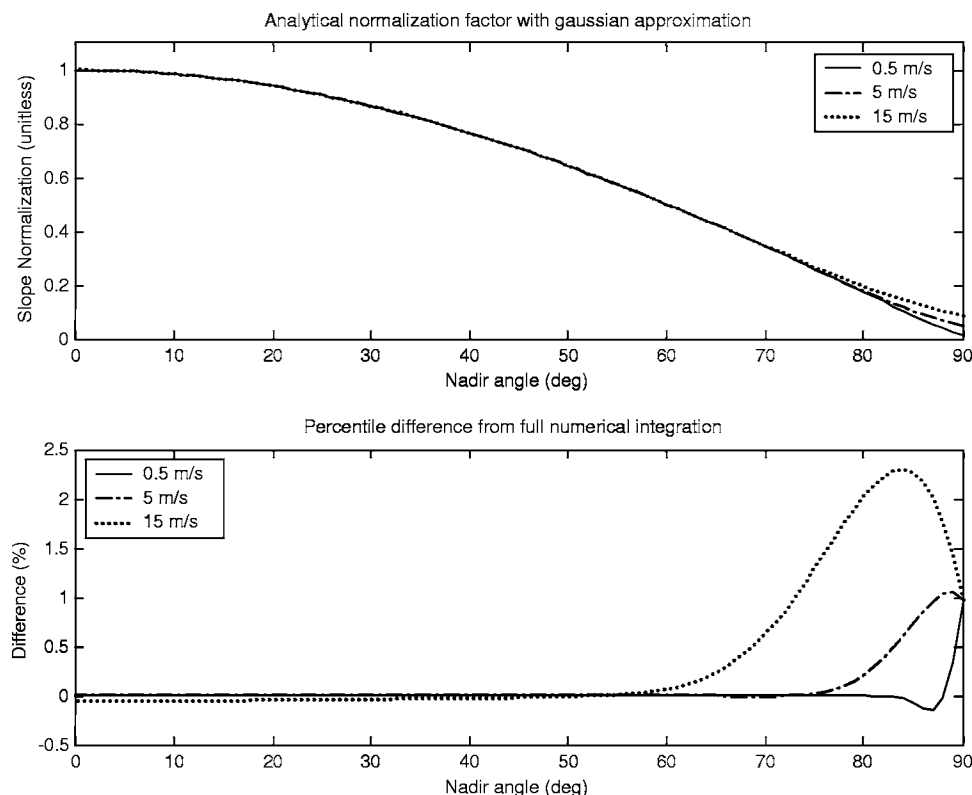

Fig. 2.   Difference in the normalizing factor from the complete solution with the Gram–Charlier PDF at different wind speeds resulting from use of the Gaussian PDF to obtain an analytical solution.
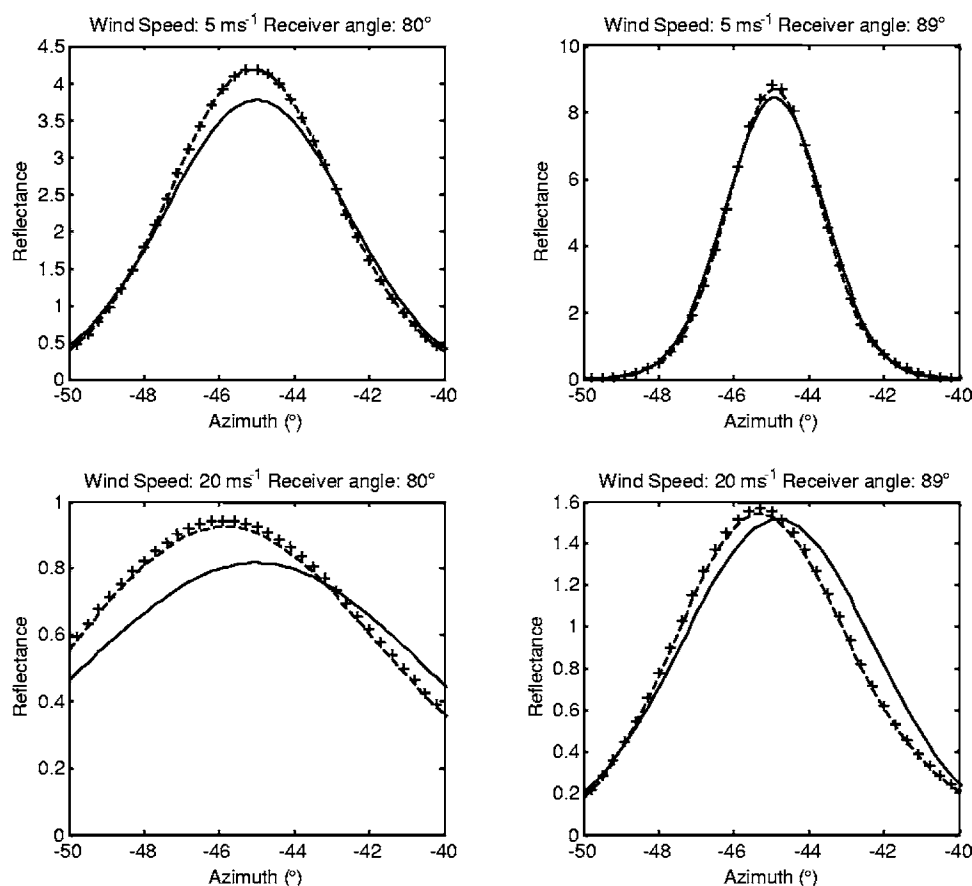
Fig. 3.   Point source (80° zenith angle) reflectance for different wind speed and receiver nadir angles. The dashed curve is the analytical solution with the Gaussian PDF in both the numerator and the normalization factor, the plus signs (+) are the exact numerical solution with the Gram–Charlier approximation, and the solid curve is the analytical solution with the Gaussian PDF in the normalizing factor only.

Table 1. Speed Comparison between Analytical and Numerical Solution at Equal Accuracy

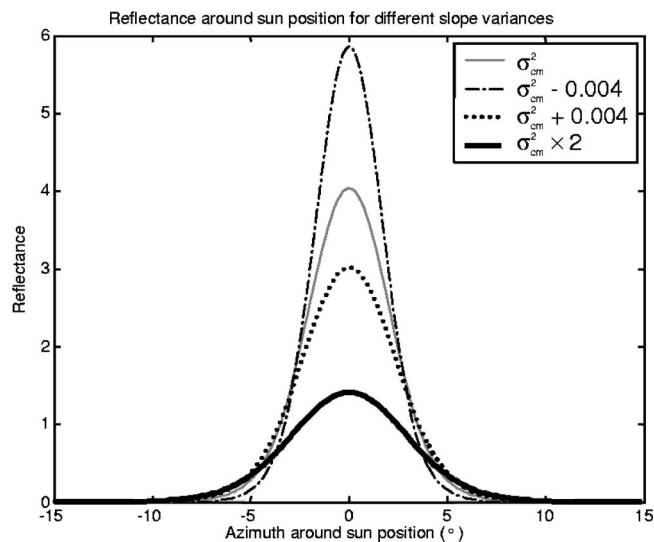| Wind Speed (m s^{-1})	Numerical Time (s)	Analytical Time (s)	Speed Factor
1	3.941	0.007.853	501.9
5	1.665	0.007.750	214.9
10	0.880	0.007.417	118.6
15	0.685	0.007.498	91.3
20	0.597	0.007.555	79.1

Fig. 4.   Variations in the reflectance of a point source located at 80° zenith angle for a detector sweeping across the source azimuth at 80° nadir angle. The wind speed is 5 m/s blowing toward the source. Variances used to obtain these results are those of Cox and Munk, Cox and Munk with its standard errors (±0.004), and Cox and Munk multiplied by two.

cous damping and wind input power, Mermelstein *et al.*[8] obtained cutoff wave vectors for a large range of wind speeds and for two water temperature extremes (0° and 30°C). According to these results, the use of the geometrical optics approximation poses no problem for wave numbers up to about 1600 m^{-1}. The analytical model can therefore be used up to the far infrared.

The largest source of uncertainty remains the slope variance models. The relationship between slope variances and various environmental factors is not fully understood. Because of this, measured upwind and crosswind slope variances, as well as the skewness and kurtosis parameters, remain rather noisy when compared with the derived empirical equations. In Fig. 4, the effect of the error of the Cox and Munk variance model (±0.004) can be seen.

Also interesting in Fig. 4 is the effect of multiplying the variance by a factor of 2.0 such as measured by Shaw and

Churnside for a Richardson number of about −0.2. It is clear that the effects of our approximations (Fig. 3) are insignificant compared to the errors stemming from the variance models. BRDF calculations would benefit greatly from a better understanding of the mechanisms that govern the sea slope variances.

7. RADIANCE CALCULATION

The sea surface radiance can now be obtained by using the expression for q_{vn} instead of p in Eq. (16). The radiance reflected from the sky and sun is calculated by using Eq. (33b) and taking into account the Fresnel reflection coefficients in the calculation of F. Similarly, the thermal radiance is obtained by using Eq. (33c) considering for F the emissivity (1−reflectance) which depends on the facet orientation.

This approach might not be practical when calculating the reflected solar radiance since only a small range of slopes can reflect the solar disk. In this case, a transformation from slope space to sky space is appropriate. This is done by using the Jacobian of the transformation[6,7]

$$d^2\zeta = \frac{\sec\omega \sec^3\theta_n \sin\theta_s d^2\Psi_s}{4} = \frac{\sin\theta_s\, d^2\Psi_s}{4z_n^3(\mathbf{U}_n \cdot \mathbf{U}_r)}. \quad (34)$$

Thence, the reflected solar radiance is obtained with

$$\bar{R}_{\text{sun}}(\Psi_r) = \frac{L_{\text{sun}}}{4} \iint\limits_{\text{sun disk}} \frac{rq_{vn}\sin\theta_s d^2\Psi_s}{z_n^3(\mathbf{U}_n \cdot \mathbf{U}_r)}, \quad (35)$$

where r is the Fresnel reflectance and is calculated along with q_{vn} for each integration point on the sun disk and L_{sun} is the average radiance of the solar disk, given that it can be approximated as being constant. Although this can be computed very quickly, it can be simplified further by approximating r and q_{vn} as being constant. Equation (35) then becomes
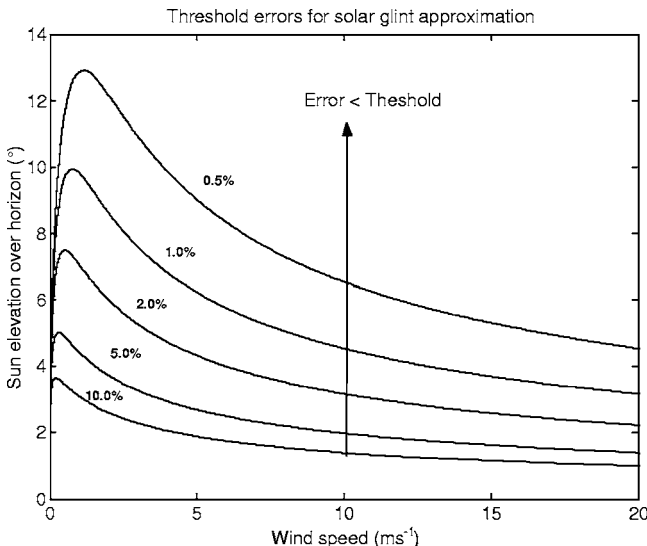

Fig. 5. Validity domain for the analytical approximation for sun glint radiance according to maximum acceptable error.

Table 2. Environmental Conditions during the Data Measurements

Time Period (LST)	8:00 −8:30 am	8:30 −9:00 am	12:00 −12:30 pm
Sun zenith angle (°)	80.9	76.4	59.4
Wind speed at 10 m(m/s)	5.2	4.4	3.9
Wind direction (° E of N)	251.6	242.7	244.5
Sun azimuth (°)	127.1	132.4	181.5
Richardson number	−0.88	−1.09	0.10

$$\bar{R}_{\text{sun}}(\Psi_r) \simeq \frac{\pi\epsilon^2 L_{\text{sun}} r q_{vn}}{4z_n^3(\mathbf{U}_n \cdot \mathbf{U}_r)}, \quad (36)$$

where r and q_{vn} are calculated according to the sun center coordinates. The validity domains of this approximation are represented in Fig. 5. The lines represent maximum percentile deviation from the numerically integrated value of Eq. (35) in the sun-elevation–wind-speed plane. Any point above a given error threshold line, as indicated by the arrow, has its maximum error below the threshold. We see that the approximation is good to within 1% for any wind speed as long as the sun is more than 10° above the horizon.

8. CASE STUDIES

Su *et al.*[5] have presented comparisons between measurements and calculations obtained using the the widely used basic BRDF model that convolves Fresnel reflectances with the Cox and Munk PDF. Here, we present simulations of sea reflected radiance using our model under the conditions that prevailed at the CERES (Clouds and The Earth's Radiant Energy System) Ocean Validation Experiment (COVE) platform (25 km off Chesapeake Bay) at the time of their observations. This allows a comparison of our model with both published measurements and a more rudimentary BRDF model. Three sets of measurements at 500 nm performed by Su *et al.* are considered, averaged half-hourly starting at 8:00 am, 8:30 am, and noon LST on January 6, 2001. A complete description of the data and instrument can be found in their paper. Meteorological and environmental data for the COVE site are readily available from the NASA Langley CERES ARM (Atmospheric Radiation Measurement) Validation Experiment (CAVE).[25,27]

The average environmental parameters for each 30 min measurement are given in Table 2. Parameters not measured directly during the experiment have been recomputed for this study and because of different methods the numbers may vary slightly from those found in the Su *et al.* paper. Scaling of wind speed from the 38 m measurement height down to 12.5 m was done using

$$U(z) = \frac{u_*}{k} \ln\left(\frac{z}{z_0}\right) \quad (37)$$

where k is the Von Karman constant ($\simeq 0.4$), u_* is the wind friction velocity and z_0 is assumed to be equal to 0.0009 as done by Su *et al.* The wind friction velocity and temperature at 10 m (used to calculate the Richardson

number) are calculated using LWKD,[28] the DRDC (Defense Research and Development of Canada) Valcartier surface layer aerodynamic model based on the Monin–Obukhov theory.

Since we are attempting to evaluate our specular BRDF model by using real radiance measurements, it is crucial that we also model as best we can all other radiance contributions. Thus, detector to surface atmospheric path radiance and subsurface scattering are added to our simulations using existing models so that their absence is not interpreted as an error in our model. Whitecaps are not considered because of the relatively low prevailing wind speeds.

The sun irradiance, sky radiances, and detector-to-surface-path radiances and transmittances at 500 nm are calculated using MODTRAN 4.0[29,30] with atmospheric profiles and aerosol optical properties modeled with WKDAER, a DRDC Valcartier aerosol extinction model.[31] Atmospheric radiance calculations are performed using the two-stream-multiple-scattering approximation. Although this approximation may cause some inaccuracies

at low sun elevations, it was chosen for its smaller computational time. A chlorophyll concentration value of 3 mg/m^3 was obtained from the SeaWiFS satellite, and the subsurface scattering by water and phytoplankton was approximated.[32,33] Maximum subsurface scattered radiance values of about 0.07, 0.13, and $0.21 \text{ mW/(cm}^2 \cdot \text{nm} \cdot \text{sr})$ for sun zenith angles of 80.9°, 76.4°, and 59.4°, respectively, were obtained. These values are significant only far from the solar glint and close to nadir viewing angles.

Sea slope variances are calculated with the Cox and Munk model [Eqs. (9)] and corrected for stability according to the Shaw and Churnside relation [Eq. (12)] in order to attain as much accuracy as possible. Equation (33b) is used to compute sky reflected radiances while Eq. (36) is used for the sun contribution.

The results of the simulations are shown in Fig. 6. The first row is the 30 min average COVE data starting at 8:00 (a), 8:30 (b), and 12:00 (c). The second row, (d), (e), and (f), shows the simulated results. The last row, (g), (h), and (i), shows azimuthal distributions of both measured
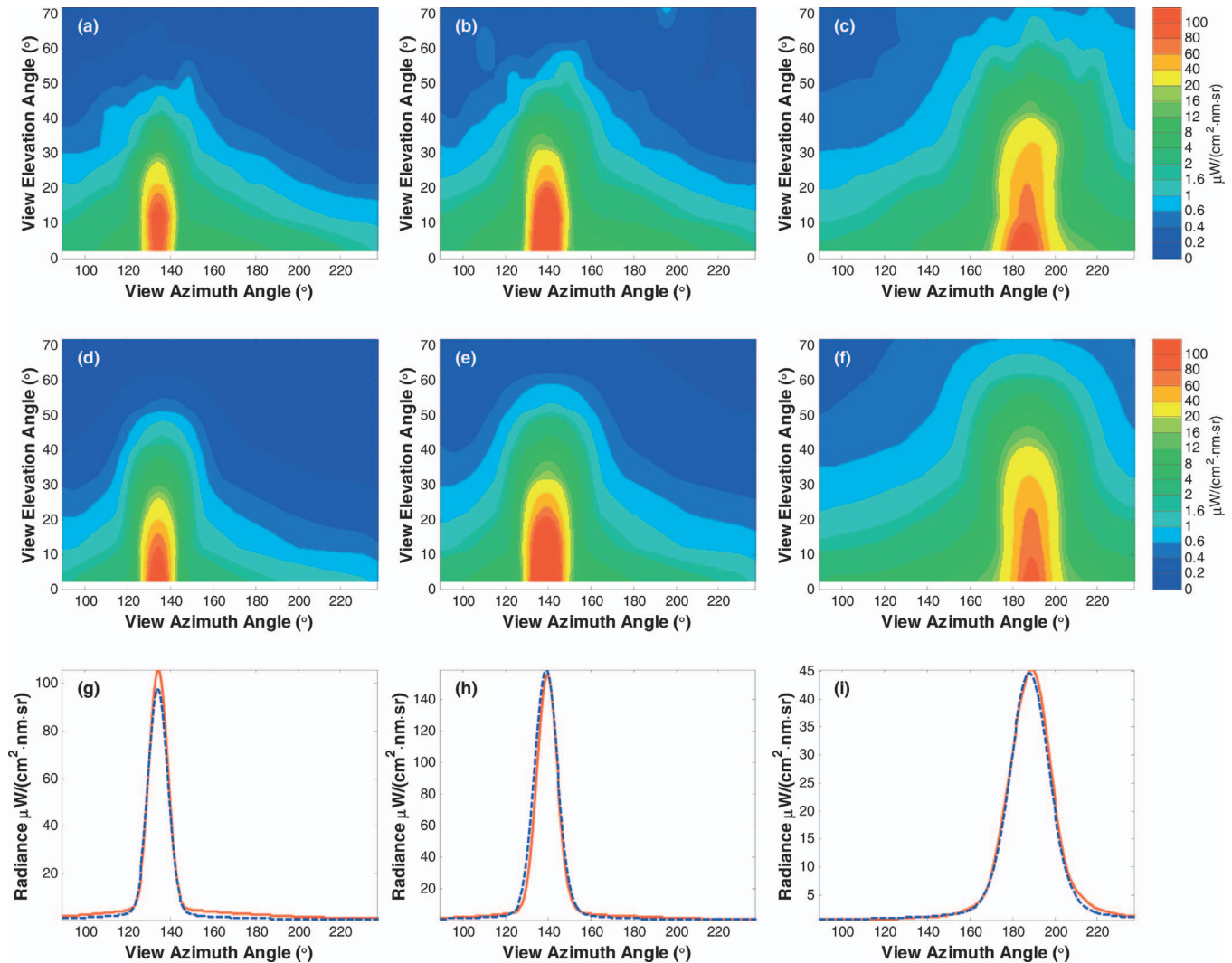

Fig. 6.   (a),(b),(c) Measured and (d),(e),(f) simulated radiances averaged over 30 min on January 6, 2001, starting at 8:00 am (first column), 8:30 am (second column), and 12:00 noon (third column). Plots on the last row (g),(h),(i) are measured (solid curve) and simulated (dashed curve) azimuthal radiance distribution at 9.1°, 13.6° and 30.6° below the horizon, respectively.

and simulated radiance at the specular elevation (the mirror angle of the sun elevation). The view elevation angles in the first two rows are absolute values relative to the horizon.

As shown in Fig. 6, the simulated radiances are in very good agreement with the measurements in both morphology and amplitude. By comparing results obtained by Su *et al.*[5] with ours, one notes that the more complex BRDF presented here yields better agreement with observations. Panes (a) and (d) of Fig. 6 are analogous to Fig. 5 in Su *et al.*, while panes (c) and (f) are the equivalent of their Fig. 6, although their figures are plotted in reflectance units. The improvement is especially noticeable for the simulation starting at 12:00 (third column). The principal discrepancies between simulations and measurements arise near the horizon when the sun is low (first two columns). In those cases, measured radiance outside the solar glint region is greater than the simulated one. This is thought to be due to errors in sky radiance calculation, and might arise from the approximation made in the multiple-scattering contributions of the incident energy.

The azimuthal distributions also seem to be improved from those modeled in Su *et al.* [panes (h) and (i) of Fig. 6 correspond to their Fig. 8]. A note of caution must be added though, since even differences in the variances as small as the error on the Cox and Munk model would yield differences in amplitude from the model as large as those seen in Su *et al.* (see Fig. 4). This is also true for small miscalculations in aerosol properties, especially at low sun elevation. Because of this, the only thing we can say with some assurance is that there is an improvement in glint morphology.

9. CONCLUSION

We presented in this paper an elaborate model to calculate the sea surface specular BRDF. Apart from the advantages of including such effects as shadowing, wave facet hiding, and weighting, the model was reduced to an analytical expression. Because of this, it is possible to calculate the reflected radiance from a wind-ruffled water surface with a significant speed improvement compared with traditional numerical evaluation. At equivalent precision, the analytical solution for the BRDF is between 100 and 500 times faster than the full numerical integration. A preliminary validation of the analytic model in the visible has yielded very good agreement with measurements and seems to constitute a real improvement compared with more basic models, at least with regard to the morphology of the sun glint pattern.

Some approximations had to be made in order to obtain the analytic form. The geometrical optics approximation is used that limits the model to wavelengths significantly smaller than 0.6 mm. Also, the Gaussian approximation to the wave slope PDF is used to normalize a probability function that makes use of the Gram–Charlier expansion. This slightly violates the restriction that a PDF should integrate to unity. Nevertheless, the error was shown to have a minor impact of the same order as numerical integration would have produced. It is worth pointing out that when put into perspective, the errors expected from our

model are small when compared with the errors that stem from the uncertainties of the slope variance models.

Further simplification permits us, in certain circumstances, to use the model to calculate quickly the solar reflected component of the sea surface radiance, or solar glint, with a compact analytical equation. An analytical form to calculate solar glint that is applicable in a wide range of circumstances and geometries can be very useful in extracting slope statistics. Our analytical model can easily be inverted to provide the PDF from sun glint radiance measurements, provided that the other radiance contributions can be subtracted accurately. Since one of the major weaknesses of our model comes directly from PDF models, it might eventually become a tool for its own bettering.

APPENDIX A

The objective of this appendix is to demonstrate formally relation (32), which is a central point of this paper. The integral we need to solve is

$$I = \int_{-\infty}^{\infty} \int_{-\infty}^{\infty} p_0(\boldsymbol{\zeta}) W(\boldsymbol{\zeta}, \boldsymbol{\Psi}_r) H_\zeta(\boldsymbol{\zeta}, \boldsymbol{\Psi}_r) \mathrm{d}^2\boldsymbol{\zeta}, \qquad \text{(A1)}$$

with terms that can be expanded from their definitions as

$$p_0(\boldsymbol{\zeta}) = \frac{1}{2\pi\sigma_x\sigma_y}\exp\left\{-\frac{\zeta_x^2}{2\sigma_x^2} - \frac{\zeta_y^2}{2\sigma_y^2}\right\},$$

$$W(\boldsymbol{\zeta}, \boldsymbol{\Psi}_r) = -\zeta_x x_r - \zeta_y y_r + z_r,$$

$$H_\zeta(\boldsymbol{\zeta}, \boldsymbol{\Psi}_r) = \Upsilon(-z_n\zeta_x x_r - z_n\zeta_y y_r + z_n z_r). \qquad \text{(A2)}$$

By their definition, functions $W(\boldsymbol{\zeta}, \boldsymbol{\Psi}_r)$ and $H_\zeta(\boldsymbol{\zeta}, \boldsymbol{\Psi}_r)$ are symmetric about the receiver vector but can have arbitrary orientation according to the (x,y) coordinate system chosen here with respect to wind direction. Because of this, the integration of Eq. (A1) to an analytic expression is not obvious. This can be remedied by rotating the coordinate system so that one of its axes is parallel to the receiver vector (x,y) components. This is achieved by applying the following transformation $\boldsymbol{\zeta} \to \boldsymbol{\zeta}'$ to the slope components

$$\zeta_{\parallel} = \zeta_x \cos\phi_r + \zeta_y \sin\phi_r,$$

$$\zeta_{\perp} = -\zeta_x \sin\phi_r + \zeta_y \cos\phi_r, \qquad \text{(A3)}$$

with the inverse transformation $\boldsymbol{\zeta}' \to \boldsymbol{\zeta}$

$$\zeta_x = \zeta_{\parallel} \cos\phi_r - \zeta_{\perp} \sin\phi_r,$$

$$\zeta_y = \zeta_{\parallel} \sin\phi_r + \zeta_{\perp} \cos\phi_r. \qquad \text{(A4)}$$

With this transformation, terms in (A2) become

$$p_0(\zeta') = \frac{1}{2\pi\sigma_x\sigma_y}\exp\left\{-\frac{a}{2}\zeta_\parallel^2 - b\zeta_\parallel\zeta_\perp - \frac{c}{2}\zeta_\perp^2\right\},$$

$$W(\zeta_\parallel, \mathbf{\Psi}_r) = -\zeta_\parallel\sin\theta_r + \cos\theta_r,$$

$$H_\zeta(\zeta_\parallel, \mathbf{\Psi}_r) = \Upsilon([-\zeta_\parallel\sin\theta_r + \cos\theta_r]\cos\theta_n)$$

$$= \Upsilon(-\zeta_\parallel\sin\theta_r + \cos\theta_r), \tag{A5}$$

where $\cos\theta_n$ can be removed since it is always positive in Gaussian statistics and where

$$a = \frac{\cos^2\phi_r}{\sigma_x^2} + \frac{\sin^2\phi_r}{\sigma_y^2},$$

$$b = \sin\phi_r\cos\phi_r\left(\frac{1}{\sigma_y^2} - \frac{1}{\sigma_x^2}\right),$$

$$c = \frac{\sin^2\phi_r}{\sigma_x^2} + \frac{\cos^2\phi_r}{\sigma_y^2}. \tag{A6}$$

In this coordinate system, Eq. (A1) can be expressed as the sum of two integrals

$$I = I1 + I2 = -\sin\theta_r\int_{-\infty}^{\infty}\int_{-\infty}^{\infty}\zeta_\parallel p_0(\zeta')H_\zeta(\zeta_\parallel, \mathbf{\Psi}_r)\mathrm{d}^2\zeta'$$

$$+ \cos\theta_r\int_{-\infty}^{\infty}\int_{-\infty}^{\infty}p_0(\zeta')H_\zeta(\zeta_\parallel, \mathbf{\Psi}_r)\mathrm{d}^2\zeta'. \tag{A7}$$

From the partial derivatives of $p_0(\zeta')$,

$$\frac{\partial p_0(\zeta')}{\partial\zeta_\parallel} = \{-a\zeta_\parallel + b\zeta_\perp\}p_0(\zeta'),$$

$$\frac{\partial p_0(\zeta')}{\partial\zeta_\perp} = \{b\zeta_\parallel - c\zeta_\perp\}p_0(\zeta'), \tag{A8}$$

it can be shown that

$$\zeta_\parallel p_0(\zeta') = \beta\frac{\partial p_0(\zeta')}{\partial\zeta_\perp} - \alpha\frac{\partial p_0(\zeta')}{\partial\zeta_\parallel},$$

$$\alpha = \frac{c}{ca - b^2}, \quad \beta = \frac{-b}{ca - b^2}, \tag{A9}$$

and with some algebraic manipulation that

$$\alpha = \sigma^2(\phi_r), \tag{A10}$$

where the expression for $\sigma^2(\phi_r)$ is given in Eq. (24). Using Eqs. (A9) and the chain derivation rule, the integrand of $I1$ in Eq. (A7) can be expanded into

$$\beta\frac{\partial}{\partial\zeta_\perp}(H_\zeta(\zeta_\parallel, \mathbf{\Psi}_r)p_0(\zeta')) - \beta p_0(\zeta')\frac{\partial H_\zeta(\zeta_\parallel, \mathbf{\Psi}_r)}{\partial\zeta_\perp}$$

$$- \alpha\frac{\partial}{\partial\zeta_\parallel}(H_\zeta(\zeta_\parallel, \mathbf{\Psi}_r)p_0(\zeta')) + \alpha p_0(\zeta')\frac{\partial H_\zeta(\zeta_\parallel, \mathbf{\Psi}_r)}{\partial\zeta_\parallel}. \tag{A11}$$

The integration of the first and third terms in relation (A11) will yield zero, since $p_0(\inf) = p_0(-\inf) = 0$ and H_ζ can

result only in 0 or 1. Also, because H_ζ depends only on $\zeta_\parallel$, the second term is null, leaving only the fourth term. Finally, since H_ζ is a Heaviside function whose transition from 0 to 1 can easily be shown to occur at $\cot\theta_r$ in the $\zeta_\parallel$ direction, and since the derivative of a Heaviside is a Dirac delta function, we have

$$\int_{-\infty}^{\infty}p_0(\zeta')\frac{\partial H_\zeta(\zeta_\parallel, \mathbf{\Psi}_r)}{\partial\zeta_\parallel}\mathrm{d}\zeta_\parallel = -\sin\theta_r\int_{-\infty}^{\infty}p_0(\zeta')\delta(-\sin\theta_r\zeta_\parallel$$

$$+ \cos\theta_r)\mathrm{d}\zeta_\parallel = -p_0(\cot\theta_r, \zeta_\perp). \tag{A12}$$

With some algebraic manipulation, p_0 can also be expressed as

$$p_0(\zeta') = \frac{1}{2\pi\sigma_x\sigma_y}\exp\left[-\frac{\zeta_\parallel^2}{2\sigma^2(\phi_r)}\right]\exp\left[-\frac{1}{2}\left\{\sqrt{c}\zeta_\perp + \frac{b\zeta_\parallel}{\sqrt{c}}\right\}^2\right]. \tag{A13}$$

Having Eqs. (A12) and (A13) at hand, $I1$ in Eq. (A7) can now be solved more easily

$$I1 = \frac{\sigma^2(\phi_r)\sin\theta_r}{\sqrt{2\pi c}\sigma_x\sigma_y}\exp\left[\frac{-\cot^2\theta_r}{2\sigma^2(\phi_r)}\right]$$

$$= \frac{\sigma(\phi_r)\sin\theta_r}{\sqrt{2\pi}}\exp\left[\frac{-\cot^2\theta_r}{2\sigma^2(\phi_r)}\right]. \tag{A14}$$

Solving $I2$ in Eq. (A7) is a much simpler matter. Since H_ζ equals 1 up to $\cot\theta_r$ in $\zeta_\parallel$ and 0 afterwards, it simply changes the limits of integration so that

$$\int_{-\infty}^{\infty}\int_{-\infty}^{\infty}p_0(\zeta')H_\zeta(\zeta_\parallel, \mathbf{\Psi}_r)\mathrm{d}^2\zeta' = \int_{-\infty}^{\infty}\mathrm{d}\zeta_\perp\int_{-\infty}^{\cot\theta_r}p_0(\zeta')\mathrm{d}\zeta_\parallel. \tag{A15}$$

The integral in $\zeta_\perp$ is done in the same way as in Eq. (A14), so that Eq. (A15) becomes

$$\int_{-\infty}^{\infty}\mathrm{d}\zeta_\perp\int_{-\infty}^{\cot\theta_r}p_0(\zeta')\mathrm{d}\zeta_\parallel$$

$$= \int_{-\infty}^{\cot\theta_r}\frac{1}{\sqrt{2\pi}\sigma(\phi_r)}\exp\left[\frac{-\zeta_\parallel^2}{2\sigma^2(\phi_r)}\right]\mathrm{d}\zeta_\parallel, \tag{A16}$$

which is easily solved using the complementary error function. The solution of $I2$ in Eq. (A7) is then

$$I2 = \left[1 - \frac{1}{2}\mathrm{erfc}\left(\frac{\cot\theta_r}{\sqrt{2}\sigma(\phi_r)}\right)\right]\cos\theta_r, \tag{A17}$$

which leads to the complete solution for our initial integral in Eq. (A1) of

$$I = \frac{\sigma(\phi_r)\sin\theta_r}{\sqrt{2\pi}}\exp\left[\frac{-\cot^2\theta_r}{2\sigma^2(\phi_r)}\right]$$

$$+ \left[1 - \frac{1}{2}\mathrm{erfc}\left(\frac{\cot\theta_r}{\sqrt{2}\sigma(\phi_r)}\right)\right]\cos\theta_r. \tag{A18}$$

In turn, using the definitions in Eqs. (23), the result in Eq. (A18) can easily be rewritten as

$$I = [1 + \Lambda(v_r)]\cos \theta_r.$$

ACKNOWLEDGMENTS

Corresponding author V. Ross's e-mail address is Vincent.Ross.AEREX@drdc-rddc.gc.ca.

REFERENCES

1. R. W. Preisendorfer and C. D. Mobley, "Albedos and glitter patterns of a wind-roughened sea surface," J. Phys. Oceanogr. **16**, 1293–1316 (1986).
2. C. Bourlier, J. Saillard, and G. Berginc, "Effect of correlation between shadowing and shadowed points on the Wagner and Smith monostatic one-dimensional shadowing function," IEEE Trans. Antennas Propag. **48**, 437–446 (2000).
3. C. Bourlier and G. Berginc, "Microwave analytical backscattering models from randomly rough anisotropic sea surface—comparison with experimental data in C and Ku bands," Electromagn. Waves **37**, 31–78 (2002).
4. B. Henderson, J. Theiler, and P. V. Villeneuve, "The polarized emissivity of a wind-roughened sea surface: a Monte-Carlo model," Remote Sens. Environ. **88**, 453–467 (2003).
5. W. Su, T. Charlock, and K. Rutledge, "Observations of reflectance distribution around sunglint from a coastal ocean platform," Appl. Opt. **41**, 7369–7383 (2002).
6. C. R. Zeisse, "Radiance of the Ocean Horizon," Tech. Rep. NCCOSC RDT&E TR-1660 (Naval Command, Control and Ocean Surveillance Center, RDT&E Division, San Diego, Calif., 1994).
7. C. R. Zeisse, "Radiance of the ocean horizon," J. Opt. Soc. Am. A **12**, 2022–2030 (1995).
8. M. Mermelstein, E. Shettle, E. Takken, and R. Priest, "Infrared radiance and solar glint at the ocean-sky horizon," Appl. Opt. **33**, 6022–6034 (1994).
9. D. Vaitekunas, "Technical manual for SHIPIR/NTCS (2.9)," Document A912-002 (Davis Engineering Limited, Ottawa, Ontario, Canada, 2002).
10. C. Cox and W. Munk, "Measurement of the roughness of the sea surface from photographs of the sun glitter," J. Opt. Soc. Am. **44**, 838–850 (1954).
11. C. Cox and W. Munk, "Statistics of the sea surface derived from sun glitter," J. Mar. Res. **13**, 198–227 (1954).
12. J. Wu, "Sea-surface slope and equilibrium wind-wave spectra," Phys. Fluids **13**, 741–747 (1972).
13. J. Wu, "Mean squared slopes of the wind-disturbed water surface, their magnitude, directionality, and composition," Radio Sci. **25**, 37–48 (1990).
14. M. A. Donelan and W. J. Pierson, "Radar scattering and equilibrium range in wind-generated waves with application to scatterometry," J. Geophys. Res. **92**, 4971–5029 (1987).
15. J. R. Apel, "An improved model of the ocean surface wave vector spectrum and its effects on radar backscatter," J. Geophys. Res. **99**, 269–16 291 (1994).
16. V. Ross and D. Dion, "Assessment of sea slope statistical models using a detailed micro-facet BRDF and upwelling radiance measurements," in Proc. SPIE **5572**, 112–122 (2004).
17. Y. Liu, M.-Y. Su, X.-H. Yan, and W. T. Liu, "The mean-square slope of ocean surface waves and its effects on radar backscatter," J. Atmos. Ocean. Technol. **17**, 1092–1105 (2000).
18. P. A. Hwang and O. H. Shemdin, "The dependence of sea surface slope on atmospheric stability and swell conditions," J. Geophys. Res. **93**, 13,903–13,912 (1988).
19. J. A. Shaw and J. H. Churnside, "Scanning-laser glint measurements of sea-surface slope statistics," Appl. Opt. **36**, 4202–4213 (1997).
20. G. Plass, G. Kattawar, and J. Guinn, "Radiative transfer in earth's atmosphere and ocean: influence of ocean waves," Appl. Opt. **14**, 1924–1936 (1975).
21. B. G. Smith, "Lunar surface roughness, shadowing and thermal emission," J. Geophys. Res. **72**, 4059–4067 (1967).
22. B. G. Smith, "Geometrical shadowing of a random rough surface," IEEE Trans. Antennas Propag. **15**, 668–671 (1967).
23. R. J. Wagner, "Shadowing of randomly rough surfaces," J. Opt. Soc. Am. **41**, 138–147 (1966).
24. M. I. Sancer, "Shadow-corrected electromagnetic scattering from a randomly rough surface," IEEE Trans. Antennas Propag. **17**, 577–585 (1969).
25. Z. Jin, T. Charlock, and K. Rutledge, "Analysis of Broadband Solar Radiation and Albedo over the Ocean Surface at COVE," Bull. Am. Meteorol. Soc. **19**, 1585–1601 (2002).
26. W. J. Plant, "A new interpretation of sea-surface slope probability density functions," J. Geophys. Res. **108**, 3295–3298 (2003).
27. D. Rutan, F. Rose, N. Smith, and T. Charlock, "Validation data set for CERES surface and atmospheric radiation budget (SARB)," World Climate Research Programme Global Energy and Water Cycle Experiment (WCRP/GEWEX) Newsletter **11**, 11–12 (International GEWEX Project Office, Silver Spring, Maryland, 2001).
28. J. L. Forand, "The L(W)WKD Marine Boundary Layer Model - Version 7.09," Technical Report 1999-099 (Defence Research Establishment of Valcartier (DREV), Valcartier, Quebec, Canada, 1999).
29. A. Berk, L. S. Bernstein, and D. C. Robertson, "MODTRAN: A Moderate Resolution Model for LOWTRAN7," Technical Report GL-TR-89-0122 (Air Force Geophysics Laboratory, Bedford, Mass., 1989).
30. P. K. Acharya, A. Berk, G. P. Anderson, N. F. Larsen, S.-C. Tsay, and K. H. Stamnes, "MODTRAN4: Multiple Scattering and Bi-Directional Reflectance Distribution Function (BRDF) Upgrades to MODTRAN," in Proc. SPIE **3756**, 19–21 (1999).
31. D. Dion, L. Gardenal, J. L. Forand, M. Duffy, G. Potvin, and S. Daigle, "IR Boundary Layer Effects Model (IRBLEM), IRBLEM5.1 documentation, DRDC-RDDC Valcartier, Quebec, Canada (2004). (Available via e-mail by submitting request to the authors.)
32. H. R. Gordon, O. B. Brown, R. H. Evans, J. W. Brown, R. C. Smith, K. S. Baker, and D. K. Clark, "A semianalytic radiance model of ocean color," J. Geophys. Res. **93**, 10,909–10,924 (1988).
33. A. Morel and B. Gentili, "Diffuse reflectance of oceanic waters. II. Bidirectional aspects," Appl. Opt. **32**, 6864–6879 (1993).